Continuous Water Vapor Profiles from Operational Ground-Based Active and Passive Remote Sensors

D. D. Turner,* W. F. Feltz,+ and R. A. Ferrare#

ABSTRACT

The Atmospheric Radiation Measurement program's Southern Great Plains Cloud and Radiation Testbed site central facility near Lamont, Oklahoma, offers unique operational water vapor profiling capabilities, including active and passive remote sensors as well as traditional in situ radiosonde measurements. Remote sensing technologies include an automated Raman lidar and an automated Atmospheric Emitted Radiance Interferometer (AERI), which are able to retrieve water vapor profiles operationally through the lower troposphere throughout the diurnal cycle. Comparisons of these two water vapor remote sensing methods to each other and to radiosondes over an 8-month period are presented and discussed, highlighting the accuracy and limitations of each method. Additionally, the AERI is able to retrieve profiles of temperature while the Raman lidar is able to retrieve aerosol extinction profiles operationally. These data, coupled with hourly wind profiles from a 915-MHz wind profiler, provide complete specification of the state of the atmosphere in noncloudy skies. Several case studies illustrate the utility of these high temporal resolution measurements in the characterization of mesoscale features within a 3-day time period in which passage of a dryline, warm air advection, and cold front occurred.

1. Introduction

The specification of the state of the atmosphere, especially the vertical distribution of water vapor, is critical for any atmospheric study. Accurate, high spatial and temporal resolution profiles of this constituent are required for many endeavors, including assimilation into mesoscale models to improve nowcasts/forecasts, radiative transfer, and transport and cloud processes research. The traditional method to determine these profiles is with in situ measurements made by radiosondes. However, radiosondes provide limited temporal resolution and have a significant cost associated with them, both in terms of expendables and the manual effort to launch them. Thus other techniques, especially remote sensing techniques, are being explored.

The Department of Energy's Atmospheric Radiation Measurement (ARM) program (Stokes and Schwartz 1994) recognized the need to have remotely sensed profiles of water vapor and temperature. This has facilitated the development of two unique instruments, as well as the necessary software, to achieve operational data products that provide this required thermodynamic information. These instruments are a Raman lidar and a high-resolution ground-based longwave (3.3 – 18.2 μm) interferometer (called the Atmospheric Emitted Radiance Interferometer or AERI). While research versions of both of these instruments previously existed in various agencies/universities, ARM's instrument development program provided the mechanism to develop both systems for them to make autonomous profile measurements in the lower troposphere throughout the diurnal cycle, allowing the instruments to be used operationally versus in an attended and/or periodic manner.

*Climate Dynamics Group, Pacific Northwest National Laboratory, Richland, Washington.
+Space Science and Engineering Center, Cooperative Institute for Meteorological Satellite Studies, University of Wisconsin—Madison, Madison, Wisconsin.
#Atmospheric Sciences Competency, NASA Langley Research Center, Hampton, Virginia.
Corresponding author address: D. D. Turner, Pacific Northwest National Laboratory, P.O. Box 999, MS K9-38, Richland, WA 99352.
E-mail: dave.turner@pnl.gov
In final form 31 December 1999.

Within the ARM project, there are multiple customers for water vapor profiles, each with their own specific requirements concerning temporal and vertical resolution, accuracy, and the number of profiling locations within the grid cell defined by the ARM Southern Great Plains (SGP) Cloud and Radiation Testbed (CART) site in north-central Oklahoma. Some scientists within the program are working to improve detailed radiative transfer models and, thus, need water vapor profiles with high vertical resolution and high accuracy near the radiometers used for validation in order to advance their science. Others, such as those developing parameterizations of water vapor in the grid cell, are more concerned with having profiles at multiple locations with reasonable temporal resolution in order to capture the gradients in the water vapor field within the grid. These two needs are addressed by the combination of the AERI instruments and the Raman lidar at the SGP site.

In this paper, we will provide an overview of each of these new instruments as well as the algorithms needed to retrieve the geophysical parameters from the data. The ARM SGP site is the home of this Raman lidar and five AERI instruments, the latter of which are arrayed over the roughly 300 km × 350 km site. Due to cost constraints, only one Raman lidar has been deployed within the SGP CART. One of the AERI instruments is located within 150 m of the Raman lidar, and a radiosonde launch site is less than 100 m from both systems at the SGP central facility. Since both the Raman lidar and the AERI profile water vapor, intercomparisons between them and radiosonde water va-

por profiles are presented, highlighting the strengths and weaknesses of each approach. To illustrate the utility of these advanced remote sensors, several case studies are shown and discussed. Subsequent papers will show results from the array of AERI instruments at the SGP site as well as the aerosol retrievals from the Raman lidar.

2. Methodologies

a. AERI

The AERI instrument, shown in Fig. 1a, is an advanced version of the high spectral resolution sounder designed and fabricated by the University of Wisconsin (Revercomb et al. 1988). The AERI is a fully automated ground-based passive infrared interferometer that measures downwelling atmospheric radiance from 3.3 to 18.2 μm (550–3000 cm^{-1}) every 8 min with a spectral resolution of 0.5 cm^{-1}. Careful attention to calibration results in an absolute calibration accuracy of better than 1% of the ambient radiance (Revercomb et al. 1993). The AERI instrument foreoptics consists of a scene mirror and two calibration blackbodies. A typical measurement cycle consists of a 3-min sky dwell period followed by 2-min dwell periods for each of the blackbodies. While the interferometer acquires an uncalibrated spectrum every 2 s, averaging reduces the radiometric noise in the measurements. The temperature of one of the blackbodies is fixed at 60°C, while the other is at ambient.
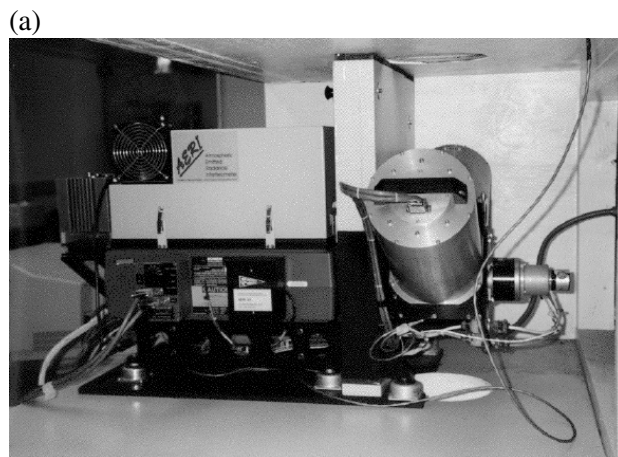
(a)

(b)

FIG. 1. Pictures of (a) the AERI and (b) Raman lidar at the ARM Southern Great Plains Cloud and Radiation Testbed site. The AERI system is 1 m × 1 m × 0.5 m in volume and weighs approximately 250 lb. The Raman lidar is housed in a 6.1 m × 2.4 m × 2.4 m seatainer.

Both the AERI calibration reference sources are high emissivity blackbody cavities containing highly accurate temperature sensors. Calibration error analysis shows that for an instrument that must operate in the open air the extrapolation of the hot-ambient calibration to the coldest scene temperatures has a comparable accuracy to a calibration that makes use of a cold target, for example, liquid nitrogen. This is because the temperature and emissivity uncertainty in reference cavities operated at or above ambient temperature can be made much smaller than those typically operated below the dewpoint temperature.

Since the AERI system performs a self-calibration every 10 min, before and after each sky view, any temperature drifts in the ambient blackbody or the internal instrument temperature are accurately accounted for. One of the advantages of using an ambient calibration point is that much of the emission the AERI is measuring is radiating from the atmosphere near the outdoor ambient temperature. This means that the calibration error of the emission from near the surface is measured very accurately with the AERI instrument.

This hot/ambient approach greatly simplifies the operations of the instrument by removing the requirement of large amounts of liquid nitrogen to provide a cold calibration source. However, since the detector (a sandwiched HgCdTe/InSb detector, providing sensitivity for 5.5–18.2 μm and 3.3–5.5 μm in channels 1 and 2, respectively) requires cooling, a solid-state Stirling cooler has been employed. An example of an AERI observed spectrum from channel 1 for two different times and very different atmospheric conditions on the same day is given in Fig. 2.

The radiance spectra contain vertical temperature and water vapor profile information above the AERI instrument as documented in Feltz et al. (1998). By inverting the radiative transfer equation, these profiles can be retrieved. However, the retrieval of water vapor and temperature from radiance data is an ill-defined problem. Smith (1970) provides an early example of how this problem was solved, and Feltz (1994) provides some background on the evolution of the retrieval technique. The retrieval technique used here was developed by Smith et al. (1999). It is an iterative technique that makes use of a first-guess profile to per-

form a physical retrieval of the temperature and water vapor profiles. The first-guess profile is derived from a statistical methodology that is based on a regression of 1159 clear radiosondes launched at the SGP CART central facility (near Lamont, OK) between 25 July 1994 and 10 May 1996 and a forward calculation at AERI spectral resolution using each of these radiosondes. The forward model is a necessary component for performing AERI retrievals in real time (within a 10-min window) and is obtained by regressing optical depth from a line-by-line transmittance model [in this case FASCODE described in Clough et al. (1981)] against parameters obtained by temperature and water vapor mixing ratio profiles. This first guess regression of temperature and moisture is very robust because it has sampled many different meteorological events that passed through the SGP CART site domain. This first guess of temperature and moisture based upon site-specific climatology is then passed through a physical retrieval algorithm described by Smith et al. (1999). The spectral regions used to perform the physical retrieval are shown in Fig. 2. Due to the strength of the IR signal at the surface from emission within the lower atmosphere, the weighting functions become quite broad at 2.5–3.0 km and thus the retrievals using only AERI data are limited to this altitude.
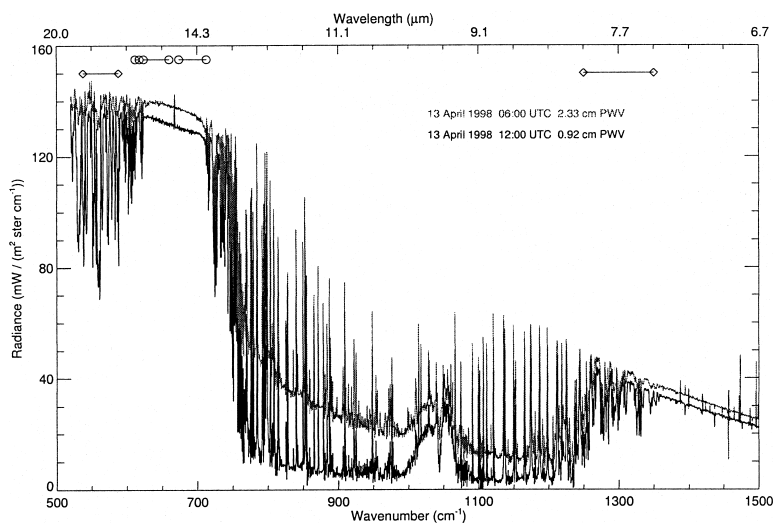

FIG. 2. Examples of two AERI spectra taken on 13 Apr 1998 before and after a dryline passage. Note the indication of a cooler temperature lapse rate in the 1200 UTC sample within the 15-μm CO_2 band (centered at 667 cm^{-1}) than at 0600 UTC. Data from 538–588 and 1250–1350 cm^{-1} (denoted with the diamonds) are used in the water vapor retrievals, while radiances from 612–618, 624–660, 674–713, and 2223–2260 cm^{-1} (the last is not shown) are used in the temperature retrievals and are denoted with circles. Large differences seen in the amplitudes of the water vapor lines indicate a drier air mass (1200 UTC) rather than smaller amplitudes (0600 UTC).

Complete tropospheric profiling can be accomplished by using physically retrieved temperature and water vapor profiles from the Geostationary Operational Environmental Satellite's (GOES) sounder brightness temperature data (Menzel et al. 1998; Xia et al. 1999). The retrieved GOES profiles serve as the first guess of the atmospheric state from the upper planetary boundary layer (PBL) (2.5 km) to the tropopause. The AERI statistical first guess is linearly blended into the GOES sounder physical retrieval between 2 and 3 km. This improves the first guess used for the AERI physical retrieval algorithm in the upper PBL, compared to statistics derived from forward model calculations alone. The GOES sounder retrievals, which use only Eta Model data in its first guess (Menzel et al. 1998), are more sensitive to the upper- and midtropospheric temperature and humidity as its weighting functions broaden out significantly toward the surface. The combination of AERI+GOES retrievals provides an excellent synergy for two reasons. The first is due to the fact that the physical retrieval algorithm used by the AERI is able to modify the profiles retrieved by the GOES in a region where the AERI's retrieval algorithm performs well, within the PBL. The second is that the AERI retrieves profiles in the rapidly changing thermodynamic structure of the PBL at 10-min temporal resolution. The GOES retrievals are hourly in the middle and upper troposphere where meteorological conditions are usually changing at a slower pace. For the GOES to retrieve temperature and water vapor profiles, the sky conditions must be clear or broken (at least four pixels in a three by three array around the central point of interest must be determined to be clear; each pixel is 10 km in resolution at the GOES subsatellite point). During some synoptic situations, high overcast conditions will prevent the retrieval of water vapor and temperature profiles from GOES data. In these cases, the statistical first guess is used to allow the AERI to profile under the cloud deck. However, if the clouds are too low (below approximately 1.0–1.5 km), the IR signal from the clouds overwhelms the weaker water vapor and temperature signatures, and thus the algorithm is unable to converge. Profiles are also not retrieved during precipitation events, which causes a hatch to close to protect the instrument's foreoptics. Figure 3a indicates the number of AERI+GOES retrievals (light gray), as well as the number of AERI-only retrievals that use the statistical first guess (dark gray), over a recent 16-month period. Also shown is the number of spectra observed by the instrument, which is roughly 5500 per month.

The nominal number of radiosonde ascents from a typical National Weather Service site, as well as the SGP central facility during nonintensive observation periods (IOPs), is 60 profiles per month.

b. Raman lidar

The basic theory of Raman lidar water vapor measurements is straightforward. Water vapor mixing ratio, $w(z)$, is defined as the ratio of grams of water vapor per kilogram of dry air. Since nitrogen is uniformly mixed through the troposphere, the mass of nitrogen per kilogram of dry air will be constant with altitude. Therefore, $w(z)$ is proportional to mass of water vapor per mass of nitrogen, which is proportional to the number density of water vapor molecules, $n_{wv}(z)$, divided by the number density of nitrogen, $n_{nit}(z)$, as given below:

$$w(z) \propto n_{wv}(z)/n_{nit}(z). \tag{1}$$

The returning signal S due to Raman scattering of some molecular species, whose corresponding wavelength after being Raman shifted from the laser wavelength λ_0 is λ, as a function of altitude z can be described as

$$S_\lambda(z) = I_0 k_\lambda z^{-2} O_\lambda(z) \sigma(z) n_\lambda(z) q(\lambda_0, z) q(\lambda, z), \tag{2}$$

where I_0 is the transmitted laser pulse energy; k_λ is a scalar factor accounting for the detector's sensitivity, telescope area, and the system gain; $O_\lambda(z)$ is the function describing the overlap of the outgoing laser beam and the detector's field of view (which is unique to each detection channel); $\sigma(z)$ is the appropriate Raman backscatter cross section; $n_\lambda(z)$ is the number density of the molecule of interest; and $q(\lambda_0, z)$ is the transmission of the outgoing laser beam while $q(\lambda, z)$ is the transmission of the returning signal. If the ratio of the signal associated with water vapor and the signal associated with nitrogen is performed, many of the terms of Eq. (2) cancel, resulting in

$$\frac{S_{wv}(z)}{S_{nit}(z)} = kO(z)\left(\frac{n_{wv}(z)q(\lambda_{wv}, z)}{n_{nit}(z)q(\lambda_{nit}, z)}\right), \tag{3}$$

where $O(z)$ is now the differential overlap function $O_{wv}(z)/O_{nit}(z)$, and k contains the various constants in (2). At atmospheric temperatures, the Raman cross sections $\sigma_{wv}(z)$ and $\sigma_{nit}(z)$ can be treated as constants

(Whiteman et al. 1992, 1993), and thus are incorporated into k. Therefore, after accounting for the differential transmission factor $q(\lambda_{wv}, z)/q(\lambda_{nit}, z)$ and $O(z)$, the resultant ratio is proportional to water vapor mixing ratio. Whiteman et al. (1992) gives details on how the differential transmission factor is determined.

Uncertainties in the Raman cross sections as well as in the optical transmission characteristics of a Raman lidar hamper precise radiometric calibration (Vaughan et al. 1988); thus an external calibration source is needed. Typically, radiosondes are used to derive the height-independent calibration factor k (e.g., Melfi et al. 1989; Ferrare et al. 1995); however, Turner and Goldsmith (1999) demonstrate a technique to calibrate to the total precipitable water vapor amount derived from a collocated two-channel water vapor microwave radiometer (MWR). To maintain this calibration operationally, an automated algorithm uses clear sky nighttime data from a 3-day window centered upon the day of interest to derive the calibration factor. For example, to determine the calibration factor for 14 April, clear sky profiles from the nighttime periods from 13 to 15 April are integrated and compared to the total precipitable water vapor retrieved from the ARM MWR (Liljegren 1995) and a single height-independent calibration value k is derived: this value is then applied to all of the Raman lidar data for 14 April. The calibration of the MWR is maintained by an automated algorithm described by Liljegren (1999) to an rms error of 0.2– 0.3 K, which translates into errors in the retrieved total precipitable water vapor amount in the vertical column to less than 0.3 mm. For data collected between April and December 1998, the calibration factor for the Raman lidar's mixing ratio profile derived by this method had a standard deviation of approximately 4%.

Ferrare et al. (1998a) and Turner et al. (2000, manuscript submitted to *J. Appl. Meteor.*) gives details on how aerosol scattering ratio, aerosol backscattering coefficient, and aerosol extinction coefficient are computed. Profiles of aerosol scattering ratio, which is the ratio

of aerosol plus molecular scattering to molecular scattering, are derived using the ratio of the signal detected at the laser-wavelength to the Raman nitrogen signal. Aerosol volume backscattering cross-section profiles are then computed using the aerosol scattering ratio and molecular scattering cross-section profiles derived from atmospheric density data. These density profiles are computed using coincident pressure and temperature profiles derived from the AERI+GOES retrievals. Aerosol extinction cross-section profiles are computed from the derivative of the Raman nitrogen signal with respect to range. The aerosol backscattering and extinction profiles derived in this manner are then used to measure profiles of the aerosol extinction–backscattering ratio. Aerosol optical thicknesses are derived by integration of the aerosol extinction profiles with altitude.

The Raman lidar at the SGP site, shown in Fig. 1b, was designed to be an operational instrument to profile atmospheric water vapor, aerosols, and clouds throughout the diurnal cycle (Goldsmith et al. 1998). It utilizes the third harmonic of the Nd:YAG to transmit laser energy outward at a wavelength of 355 nm with a pulse energy of 350–400 mJ and a repetition rate of 30 Hz. It is a three spectral channel lidar, observing the backscattered light associated with
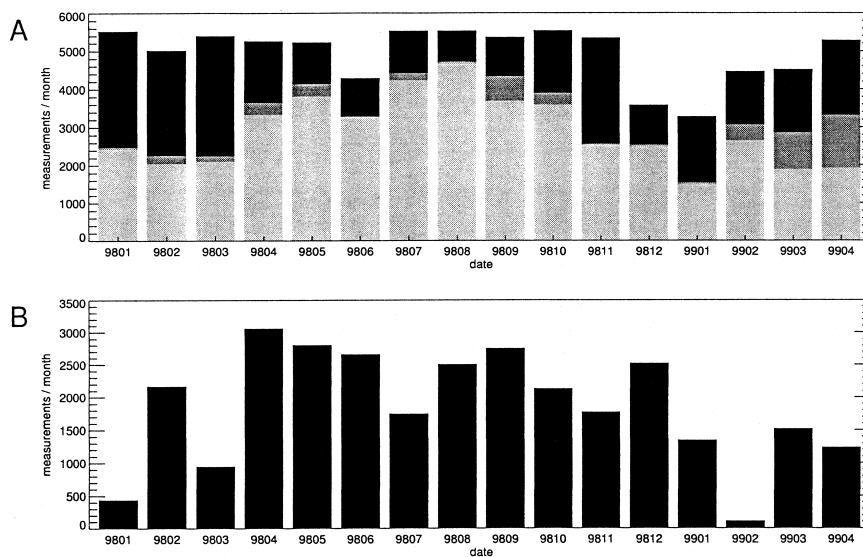

FIG. 3. (a) The number of AERI spectra (8-min resolution) in black, AERI-only retrievals (dark gray), and AERI+GOES retrievals (light gray) per month for Jan 1998–Apr 1999. The primary reasons for a retrieval not being performed are low clouds (below approximately 1.0–1.5 km) or precipitation events. (b) The number of 10-min Raman lidar profiles per month over the same period. A UPS was installed Feb 1999 to increase the number of profiles per month, as frequent power bumps at the rural site were shutting down the system. However, laser problems hampered operations in Mar and Apr 1999. The typical number of radiosonde profiles launched at the SGP central facility during normal operations for a given month is approximately 60.

Rayleigh–Mie scattering at the laser wavelength, as well as the Raman-shifted wavelengths associated with water vapor (408 nm) and nitrogen (387 nm). The raw data are collected to 0.26-ms bins, resulting in 39-m vertical resolution, and stored at 1-min intervals (the accumulation of approximately 1740 shots). During postprocessing, the vertical and/or temporal resolution can be degraded to improve the signal-to-noise ratio.

While Raman lidars have shown excellent capability of profiling water vapor and aerosols at night (Melfi et al. 1989; Ferrare et al. 1992, e.g.), the inherently weak Raman signal, especially from water vapor, together with the strong solar background makes these daytime measurements troublesome. An analysis of different possible approaches led to the decision to build the dual field-of-view system that is currently at the CART site (Goldsmith et al. 1998). The narrow field of view (~0.3 mrad) together with the narrowband interference filters (0.4 nm) work to greatly reduce the solar background by rejecting out-of-scene and out-of-band radiation. This enables the system to profile water vapor and aerosols continuously throughout the diurnal cycle.

Since the lidar was intended to be operational, it was designed to operate unattended, and the only manual requirement is periodic cleaning of the enclosure's window. Some minor manual intervention is needed at system startup, requiring about 5–10 min of the operator's time. It also requires clear sky so that the system can automatically optimize the alignment of the laser in the detector's field of view. However, fairly frequent power bumps, that is, momentary interruptions or fluctuations in power, at the rural Oklahoma site shut the lidar down by triggering the laser's safety interlock. This has resulted in significant amounts of downtime, as these bumps often occur when the site is unmanned or during periods of low overcast conditions, which can prevent restart for days at a time. The Raman lidar was operational over 50% of the time between January 1998 and April 1999. Figure 3b illustrates the number of 10-min profiles retrieved from the Raman during this period. Note that the maximum number of 10-min profiles per month is approximately 4300. In February 1999, a large uninterruptible power supply (UPS) was installed, which should greatly increase the system's uptime by eliminating the downtime associated with power bumps.

Besides these two methods, the other more traditional way to obtain profiles of temperature and water vapor is via the periodic launching of radiosondes.

Routine operations at the central facility of the SGP CART site during 1998 included the launch of three Vaisala RS-80 H-humicap radiosondes per day (at 0000, 1200, and 2000 UTC) Monday through Friday. Periodic IOPs increase the number of launches to eight per day (at 3-h intervals) 7 days per week at this facility. There were two 3-week IOPs from April to December 1998.

3. Comparisons

The two remote sensing methods were able to retrieve profiles of water vapor (temperature and aerosol also, depending on the system) approximately 60% of the time for the Raman lidar and almost 75% of the time for the AERI, for the period between April and December 1998. This resulted in almost 22 000 10-min profiles from the Raman lidar and approximately 33 000 8-min profiles from the AERI during this period. Comparatively, there were about 1000 radiosondes launched from the SGP central facility during this period. The higher temporal resolution of the two remote sensing techniques enables them to better describe the thermodynamic state of the atmosphere than radiosondes, especially when the water vapor field is changing rapidly. For example, Fig. 4 shows a dryline that passed over the central facility on 13 April 1998 that was observed by all three measurement systems. The three radiosondes that were launched around this event, at 2330 UTC on 12 April (not shown), 1130 and 2330 UTC on 13 April (Fig. 5), are too sparsely distributed in time to capture the structure of this passage. However, this structure was captured in detail by the active and passive remote sensors with good qualitative agreement. The primary contrast between the two retrieval methods used to measure the water vapor fields is vertical resolution. The Raman lidar is measuring returning photons from specific distances while the AERI retrieval algorithm is determining the average temperature and moisture values within larger slices of the atmosphere than the Raman lidar.

Examples of the individual vertical water vapor profiles from each technique compared to one another at radiosonde launch time are given in Fig. 5. Figure 5 shows comparisons on 13 April 1998 (Fig. 4) at 1131 and 2333 UTC, when the two radiosonde launches occurred on that day. The first profile comparison shows good agreement between all the water vapor sensing techniques, with the scaled radiosonde (which is scaled such that its integrated water vapor profile

matches that observed by the collocated MWR) agreeing better to both the Raman and AERI+GOES profile data than the normal radiosonde. Twelve hours later the water vapor amounts have increased and the characteristics of each methodology are present. The Raman lidar and MWR scaled radiosonde data are in very good agreement. The AERI+GOES water vapor structure and depth are not in as good agreement, due to the decreasing vertical resolution with height, and thus the gradient of water vapor at 2 km at 2333 UTC on 13 April is smoothed through and some of this moisture is erroneously placed nearer to the surface to satisfy the radiance. Figure 5 also shows similar comparisons for 14 April 1998 with the indication of rapid moisture advection in a 3-h period between 2028 and 2337 UTC increasing from 6.5 to 10 g kg^{-1} of water vapor mixing ratio on average. The 2028 UTC plot indicates that achieving close agreement between several different instruments is challenging given the variation of water vapor in time and space on any particular day. A 1 g kg^{-1} scatter within the water vapor profile comparisons indicates general agreement in vertical tendency especially between Raman, scaled radiosonde, and AERI+GOES profiles. By 2337 UTC the mixed layer is well developed to approximately 1.3 km according to the profiles; however, there is a 2 g kg^{-1} scatter in absolute mixing ratio between the measurements. AERI+GOES agrees with the scaled radiosonde the best with the Raman lidar, indicating approximately 1 g kg^{-1} drier amounts throughout the mixed layer. The large difference between the Raman lidar and the MWR scaled radiosonde profiles is explained by the fact the only
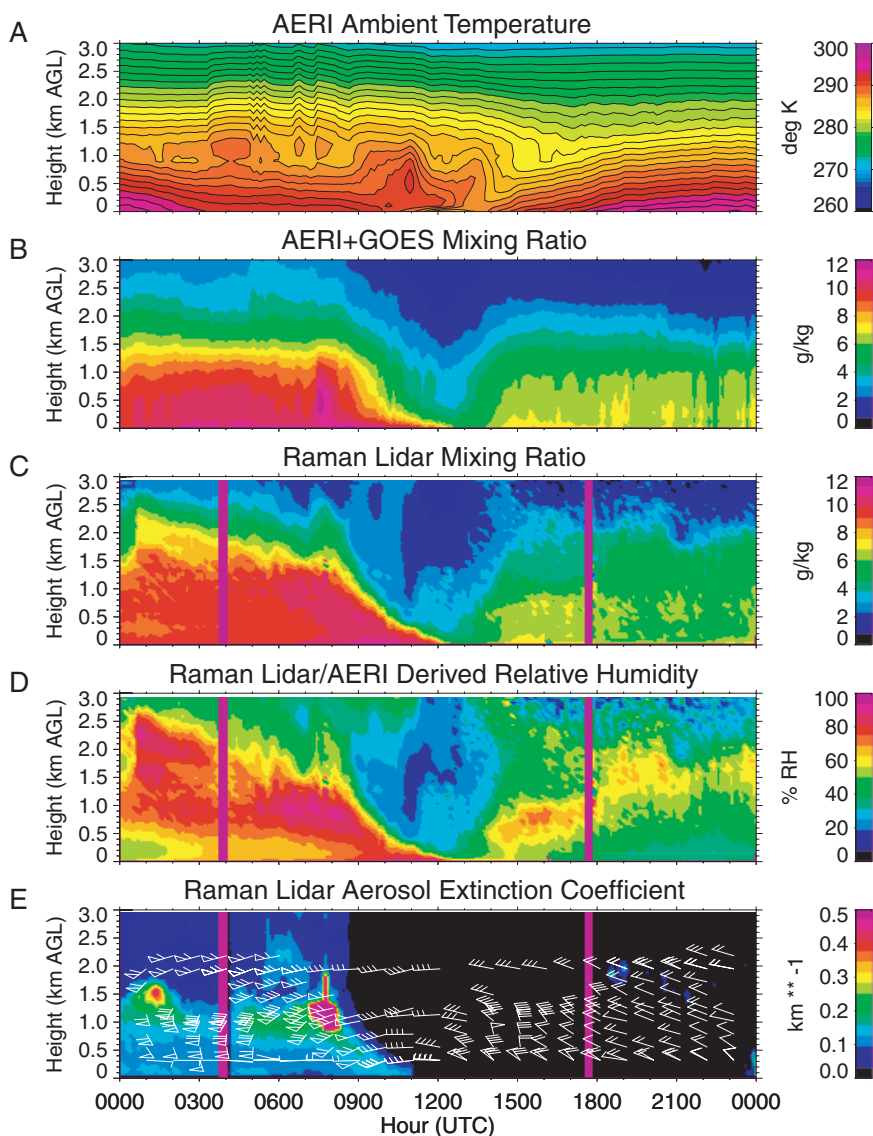

FIG. 4. Time–height cross sections of ambient temperature derived from (a) the AERI, water vapor mixing ratios derived from the (b) AERI+GOES and (c) Raman lidar, (d) relative humidity derived using AERI temperature and Raman lidar mixing ratio data, and (e) aerosol extinction from the Raman lidar for the 13 Apr 1998 dryline case. Wind data from a collocated 915-MHz wind profiler is overplotted on the aerosol data. Both the AERI+GOES and the Raman lidar retrievals are at 10-min resolution. The synoptic dryline passage is very evident between 0800 and 1200 UTC as a gradual drying from 2 km to the surface [(b) and (c)] correlated with a westerly wind and reduction in aerosol amount in (e). Notice the passage had very little impact upon the temperature field in (a).

nighttime data are used to derive the lidar's calibration factor, and that the system might still be reaching an equilibrium point after the restart due to the power bump. These profile comparisons present some of the issues involved with comparing the individual instrument profiles to one another.

Statistical intercomparisons were performed to compare each methodology with the others. For this

13 Apr 1998 1131 UTC

Raman lidar
AERI+GOES
Normal sonde
MWR scaled sonde

13 Apr 1998 2333 UTC

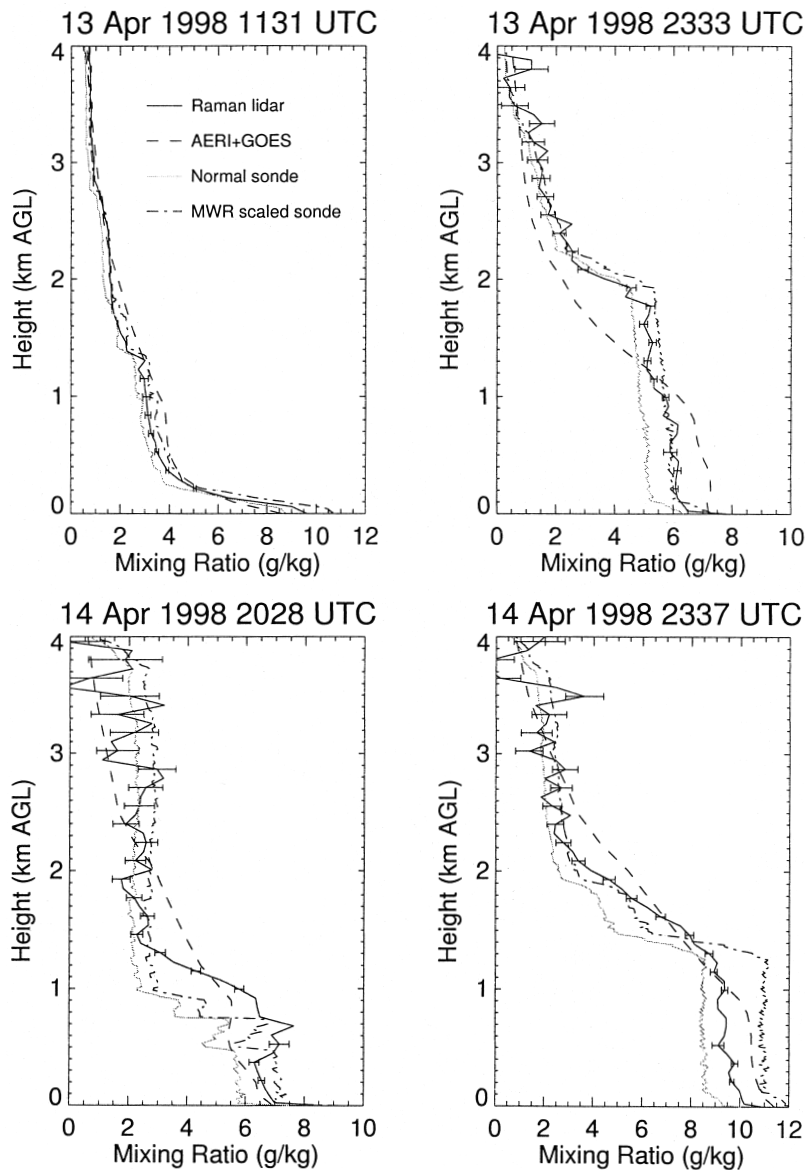## 14 Apr 1998 2028 UTC

14 Apr 1998 2337 UTC

FIG. 5. Plot of vertical profiles from the Raman lidar, AERI+GOES, normal radiosonde, and MWR scaled radiosonde mixing ratio. The upper two panels show the profile comparison collocated with the two radiosondes launched on 13 Apr 1998, while the two lower panels are from the next day. The Raman lidar profiles have 10-min temporal resolution.

exercise, clear sky samples between April and December 1998 were selected. The radiosonde and Raman lidar profiles were then degraded in vertical resolution to match the vertical resolution of the AERI+GOES retrievals (100 m from the surface to 1 km, with a gradual degradation to 250 m at 3 km). The nearest profiles within ±10 min between any two techniques were used to calculate both a mean fractional difference profile and an rms difference profile. Diurnal calibration characteristics have been reported for radiosondes, wherein daytime sondes appear 3%–5%

drier than sondes launched at night (S. Clough 2000, personal communication; Turner et al. 1998). The cause for this radiosonde phenomenon is not known. The lidar profiles could also contain a diurnal characteristic due to the large difference in solar background (Turner and Goldsmith 1999). Therefore, these results were separated into nighttime (0000–1200 UTC, or 1900–0700 local time) and daytime (1200–2400 UTC) cases for this analysis.

Figure 6 shows the mean fractional difference and rms difference between the water vapor mixing ratio profiles from radiosondes and the AERI+GOES retrievals over this period. There were 162 nighttime cases (dashed lines) and 292 daytime cases (solid lines) in the ensemble statistics. The mean fractional difference profiles show a difference of 5%–10% between the daytime and nighttime results below 1.5 km, but the diurnal differences between 1.5 and 2.5 km are negligible. The daytime result shows that the AERI+GOES retrievals are moister than the sondes by approximately 10% throughout the lower troposphere. This is consistent with the diurnal feature of radiosondes discussed above. The rms's for the daytime and nighttime cases are almost identical, with a maximum rms between the surface and 3 km of 1.5 g kg^{-1}

Similar statistics between the Raman lidar and the radiosondes are shown in Fig. 7. For this analysis, there were 91 nighttime and 49 daytime cases. A very large (10% or approximately 1 g kg^{-1}) difference is seen between the daytime and nighttime results, indicating that the sondes are significantly drier than the Raman lidar in the daytime compared to nighttime. This agrees in sign and approximate magnitude with the findings of S. Clough (2000, personal communication) and is consistent with the AERI+GOES statistics described above. For both day and night, the lidar is moister than the radiosondes, with a relatively constant offset in each. Due to the solar background, the Raman lidar's signal-to-noise
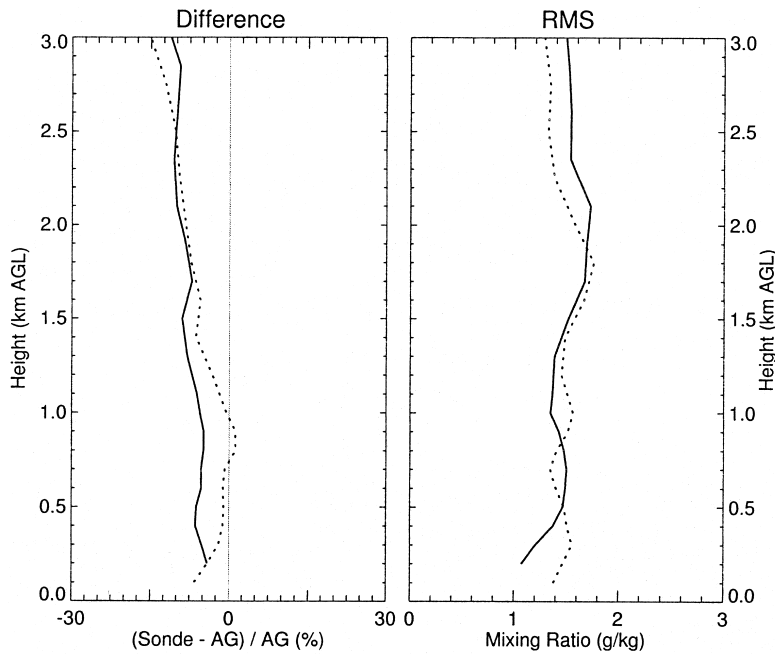
FIG. 6. Mean fractional difference (left) and rms difference statistics (right) as a function of height for AERI+GOES (AG) water vapor mixing ratio vs normal radiosondes to 3 km, broken into nighttime (dashed line) and daytime (solid line) clear sky cases. There are 162 and 292 cases in each ensemble, respectively.

have shown that when the water vapor mixing ratio profile from the radiosonde is scaled such that its integrated precipitable water vapor amount matches that retrieved from a microwave radiometer, not only is the variability of the radiosondes reduced but the diurnal calibration feature of the radiosondes is also eliminated. Therefore for the above comparisons, we have scaled the radiosondes such that the radiosondes' integrated water vapor amounts match the water vapor burden retrieved from CART MWR, and repeated the analysis above. The differences between the scaled sondes and the AERI+GOES retrievals, and the scaled sondes and the Raman lidar, are shown in Figs. 8 and 9, respectively. In both comparisons, the differences between the daytime and nighttime residuals are significantly reduced, essentially removing the diurnal difference in the residuals. The overall bias between the scaled sondes and the remote sensors is also reduced significantly, with differences less than 5% for most altitudes below 3 km. Note the especially large drop in the daytime rms between the sondes and

ratio in the daytime is much smaller than at night, but is typically greater than 10 below 3 km (this is highly dependent on the amount of water vapor present). The relatively small nightly rms profile indicates how well the lidar captures the same structure as the in situ sensor. However, the larger daytime rms profile indicates that there is significantly more variability in one or both of the sensors during the daytime.

In addition to the diurnal calibration feature, radiosondes have other limitations. A dry bias in the Vaisala radiosondes, which is attributed to contamination of the capacitive sensor due to outgassing of the packaging, is known (Guichard et al. 2000). This bias is a function of the age of the sonde package and relative humidity, but not as a function of the time of day (or solar zenith angle) of the launch time, and thus does not explain the diurnal characteristic. Additionally, Lesht and Liljegren (1996) and Lesht (1997) have shown that there can be quite large differences among radiosondes from different calibration lots. Turner et al. (1998) and Clough et al. (1999)
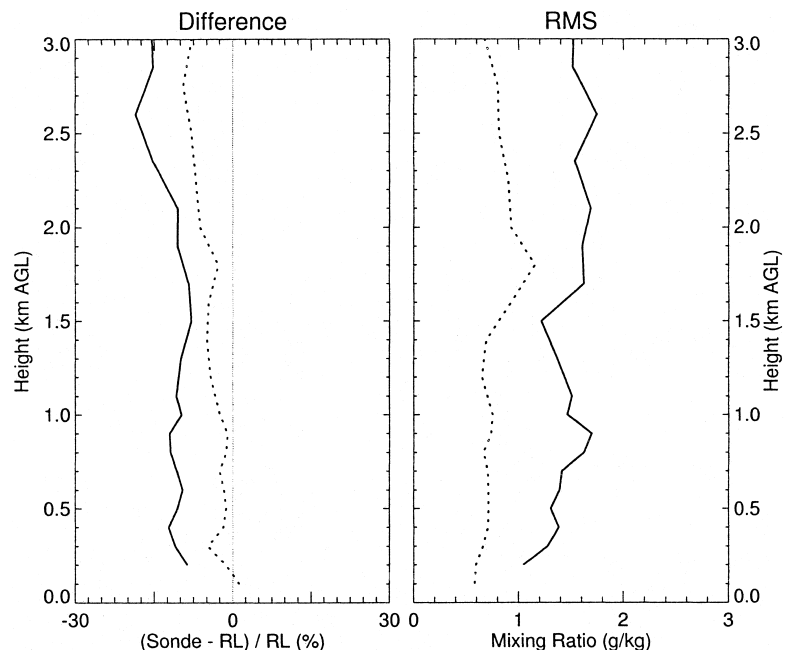

FIG. 7. Mean fractional difference (left) and rms difference statistics (right) as a function of height for Raman lidar (RL) water vapor mixing ratios vs normal radiosondes, broken into nighttime (dashed line) and daytime (solid line) clear sky cases. There are 91 and 49 cases in each ensemble, respectively.
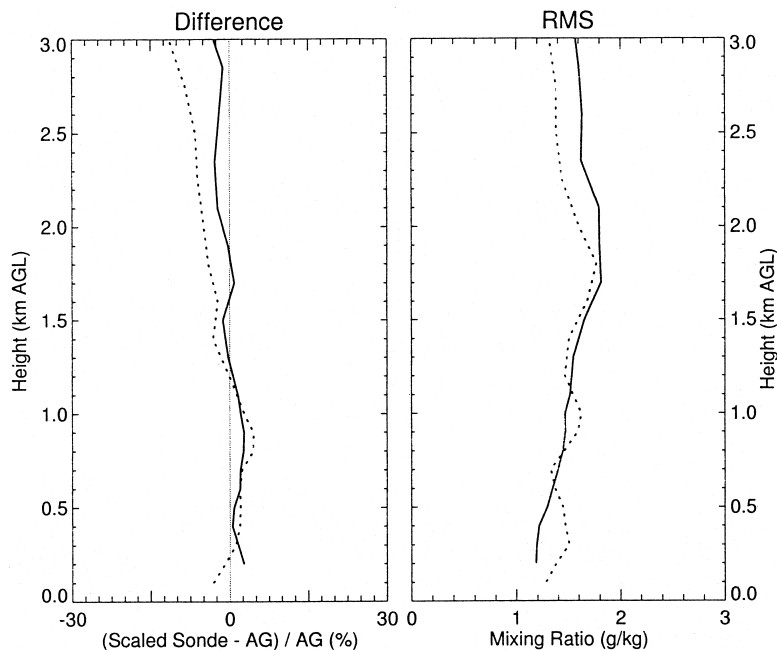
FIG. 8. Same as for Fig. 6 except that the radiosondes were scaled to agree with the integrated precipitable water vapor with the microwave radiometer.
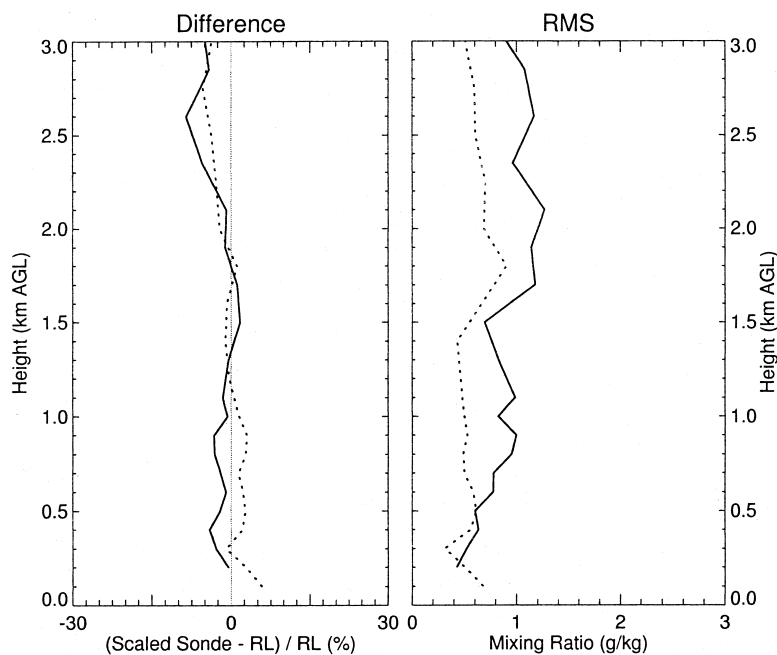

FIG. 9. Same as for Fig. 7 except that the radiosondes were scaled to agree with the integrated precipitable water vapor with the microwave radiometer.

passive remote sensor (AERI+GOES). For this analysis, there were 6017 night and 2749 daytime clear sky cases. The mean nighttime differences is 5% or smaller for all levels below 3 km. During the daytime, the mean difference is less than 10% up to about 1.7 km, above which it gradually increases. This is probably due to the declining signal-to-noise ratio in the Raman lidar data combined with the decreasing sensitivity of the AERI at these altitudes. The rms profiles are similar in shape and are slightly larger than the rms profiles comparing the AERI+GOES retrievals to the radiosondes. This indicates that the high vertical resolution structure of the water vapor field is not as well captured by the passive AERI system as it is by the in situ or active systems. Therefore, the trade-off between the passive AERI system and active Raman lidar is essentially cost and portability versus vertical resolution, since they are of both similar time resolution.

4. Case studies

The Raman lidar and AERI systems have captured numerous examples of dynamic weather events. The three cases selected below illustrate both systems' utility in monitoring atmospheric state at high temporal resolution and their complementary nature. These three events were captured during a continuous 3-day period testifying to the value of operational high temporal resolution boundary layer profiling. Each day had unique mesoscale and synoptic meteorological features of interest. The first case study is of a synoptically forced dryline passage on 13 April 1998, indicating the importance of the Raman lidar water vapor mixing ratio validating the passive AERI+GOES water vapor retrieval technique. On 14 April 1998, a Gulf of Mexico "return flow" event, wherein moisture returns to the Great Plains from the Gulf of Mexico on the western side of a high pressure system, occurred indicating the rapid nature of the water vapor advection and the fine

Raman lidar in Fig. 9—this large drop indicates that the variability of the calibration in the radiosondes launched in the daytime was especially significant.

Figure 10 shows the comparison statistics between the active remote sensor (the Raman lidar) and the

temporal scale structure of such an event. A cold frontal passage on 15 April 1998 was selected as the third example primarily to show the complementary attributes of combining the temperature field from AERI used in conjunction with the higher vertical resolution water vapor and aerosol fields from the Raman lidar. The synoptic features at the surface in the SGP domain for this 3-day study are presented in Fig. 11.

a. 13 April 1998 dryline passage

The CART Raman lidar is offering an excellent source of validation for the AERI retrieval water vapor product since it is of similar time resolution and higher vertical resolution. Figure 4 shows time–height cross sections of ambient temperature from the AERI retrievals (panel a), water vapor mixing ratio from the AERI+GOES retrievals (panel b) and Raman lidar (panel C), relative humidity derived using the lidar's water vapor data together with the temperature derived from the AERI (panel d), and aerosol extinction derived from the Raman lidar (panel e). The Raman lidar data shown have 10-min resolution. The dryline passage occurred at the central facility near Lamont, Oklahoma, between 0800 and 1200 UTC with rapid drying occurring within the boundary layer from the surface to 2 km. Passage of the dryline was also indicated by wind data from a collocated 915-MHz wind profiler (Weber et al. 1990) veering westerly from the surface to 2 km. Both the passive and active retrieval techniques showed quantitatively similar drying in the boundary layer during this period. This case provides excellent validation for the AERI retrieval technique as the Raman lidar profiles are of higher vertical resolution and time resolution compared to radiosonde data. This validation provides a way to refine the retrieval algorithm translating to improvement in the retrievals at the other four AERI instrument sites within the ARM SGP domain. The AERI spectra in Fig. 2 from 0600 and 1200 UTC on this day illustrate the large change in the emitted longwave radiance as this synoptic feature passes over the site. Notice the differences in the temperature and water vapor spectral regions at the two times indicated within the figure. Figure 4a shows the AERI retrieved ambient temperature time–height cross section, which indicates some differences in the ther-
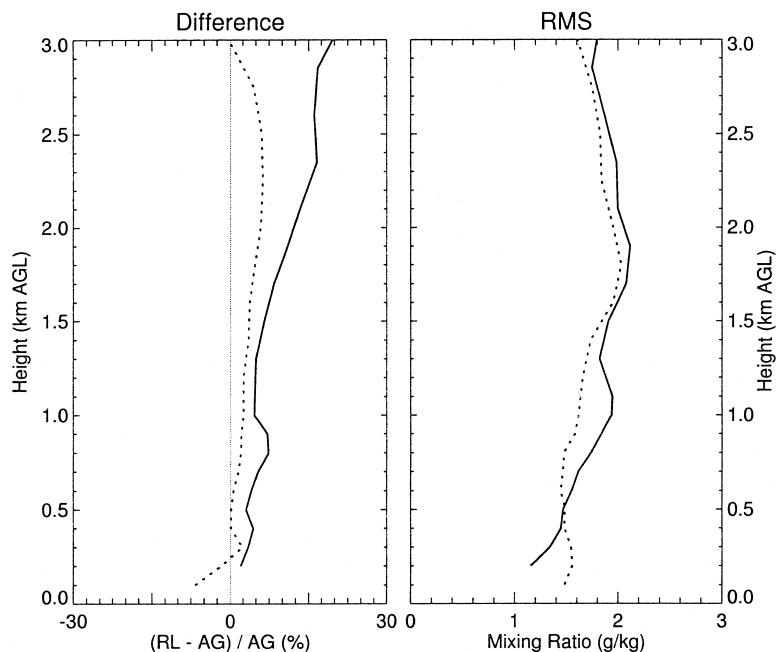

Fig. 10. Mean fractional difference (left) and rms difference statistics (right) as a function of height for AG water vapor mixing vs RL; broken into nighttime (dashed line) and daytime (solid line) clear sky cases. There are 6017 and 2749 cases in each ensemble, respectively.

mal air masses on either side of the moisture discontinuity; however, the primary contrast which highlights the passage of the dryline is in the moisture field (Figs. 4b and 4c) and in the aerosol data retrieved from the Raman lidar (Fig. 4e). Smith et al. (1998) have shown the rms difference between the AERI+GOES and radiosonde temperature profiles is less than 1 K. The aerosol extinction data show the sharp contrast in the two air masses. Figure 4 shows that rapid changes in water vapor mixing ratio and aerosol extinction are often highly correlated. Since water vapor mixing ratio is a conservative parameter for processes that do not involve condensation or evaporation, the water vapor mixing ratio can often be used to determine if variations in aerosol extinction are due to the advection of different aerosol concentrations, or rather to changes in the aerosol physical characteristics caused by hygroscopic growth (Ferrare 1997). This can be studied by examining periods where the mixing ratio is fairly constant over both time and altitude, yet the relative humidity and aerosol extinction is changing, such as between 0230 and 0330 UTC from 500 to 1500 m on this day. However, the rapidly changing air mass over the instrument due to the dryline passage hinders this sort of analysis for a large portion of this day.

Another measurement, which was compared to the water vapor profiles for both systems, is the total in-

tegrated water vapor from the microwave radiometer. A time series of integrated water vapor for this day is plotted in Fig. 12a for the microwave radiometer,

SFC TD[F] at 12 UTC on 13 Apr 1998

SFC TD[F] at 12 UTC on 14 Apr 1998

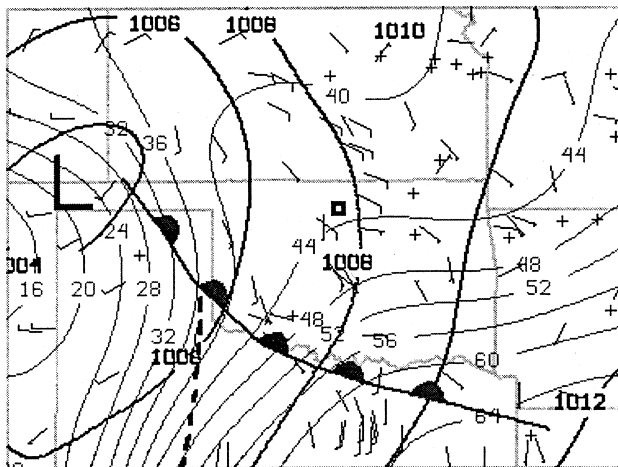SFC TD[F] at 12 UTC on 15 Apr 1998

GOES sounder, AERI+GOES, Raman lidar (at 1-min resolution), and Vaisala radiosondes. This comparison portrays the rapid decrease in water vapor between 0800 and 1200 UTC with the dryline passage. The lidar, AERI+GOES, and microwave radiometer compare well with one another on this day. Considering the GOES retrievals are an average 36 km by 45 km integrated water vapor, the hourly trends are observed very well by the satellite measurement. The AERI retrieval uses the GOES measurement within its first guess as a priori information and it is readily apparent the retrieval converts a synoptic-scale measurement to one that is mesoscale. The Vaisala radiosonde dry bias is also evident at 1200 and 2330 UTC on this day.

### b. 14 April 1998 warm air advection (return flow)

On 14 April 1998, the day following the dry line passage, rapid warm air and moisture advection occurred between 1700 and 2400 UTC. Figure 13 shows time–height cross sections of AERI+GOES potential temperature (panel a), AERI+GOES water vapor (panel b), Raman lidar water vapor (panel c), Raman lidar and AERI+GOES derived relative humidity (panel d), and Raman lidar aerosol extinction coefficient (panel e) between 1200 and 0400 UTC. The resolution of the water vapor data from the Raman lidar is the maximum 1-min 39-m resolution, which allows the finescale structure of the atmosphere to be seen, albeit at a lower signal-to-noise ratio. The Raman lidar aerosol retrievals have 10-min resolution. A power bump occurred at 0100 UTC at the site that took the Raman lidar offline for the following 13 h. From Fig. 13, we note the fine structure of the water vapor field as the advection occurs especially between 1600 and 2300 UTC. Notice the pulses of moisture in the AERI+GOES and Raman lidar time cross section between 1600 and 2300 UTC. There may be some question about the physical nature of these features. However by plotting the integrated water vapor from AERI+GOES retrievals, Raman lidar, and the microwave radiometer for this day (Fig. 12b), the water vapor fluctuation tendencies are highly correlated. Section 3 provides a possible explanation for the ap-
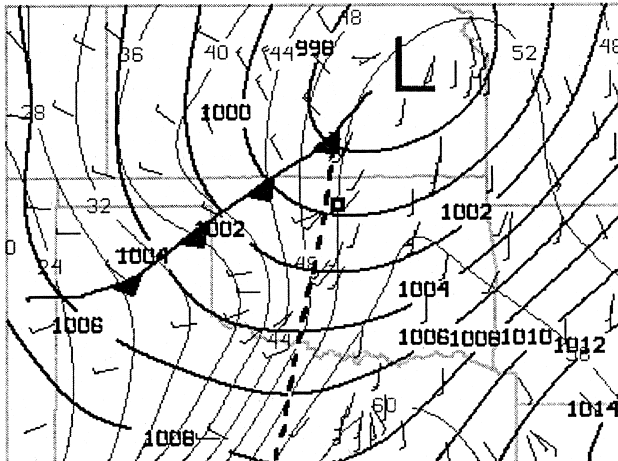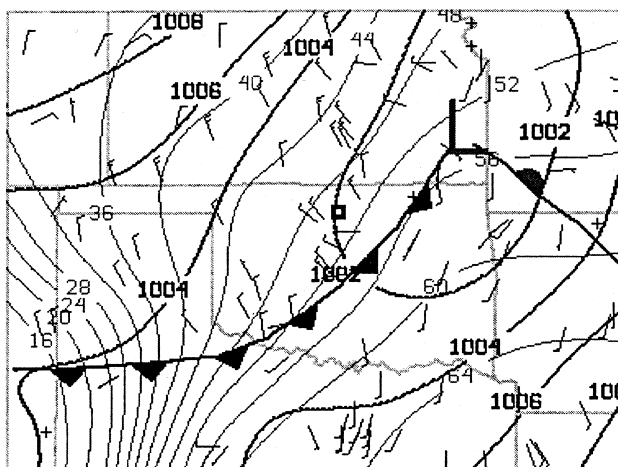
FIG. 11. Surface analysis for 1200 UTC on 13–15 Apr 1998 for the region around the SGP CART site. The central facility, where the Raman lidar and the AERI are stationed, is indicated with the dark square. Dark contours mark the isobars (mb), while gray contours denote the dewpoint isopleths (°F). The dark dotted line indicates the location of the dryline.

parent dry bias in the Raman lidar data with respect to the MWR data on this day. All systems show 1–2-mm fluctuations of integrated water vapor during this event on the timescales of tens of minutes. We speculate that this phenomenon may be due to the combination of local moisture sources, such as the flux from vegetation, and the mixing of dry and moist air within the dry convective plumes of the PBL. Monitoring return flow moisture depth and quantity at high temporal resolution is important for quantitative precipitation forecasting and the initiation of severe convection. Currently, the primary operational means to monitor the depth of return flow moisture from the Gulf of Mexico is with radiosondes launched twice per day. In a future paper, we will highlight the exciting new possibilities for calculating observed moisture divergence, convergence, and flux at high time resolution using the network of five AERI systems in the Southern Great Plains.

c. 15 April 1998 cold frontal passage

A cold frontal passage was observed on 15 April 1998 between 0900 and 1100 UTC at the central facility near Lamont. Figure 14 shows time–height cross sections of AERI temperature retrievals (panel a), AERI+GOES and Raman lidar water vapor mixing ratio profiles (panels b and c), the derived relative humidity profiles using the lidar's mixing ratio data with the AERI retrieved temperature data (panel d), and the aerosol extinction profiles from the Raman lidar (panel e).

The cold frontal passage is indicated within the AERI temperature field (Fig. 14a) as a rapid cooling and as a drying within the AERI+GOES and Raman
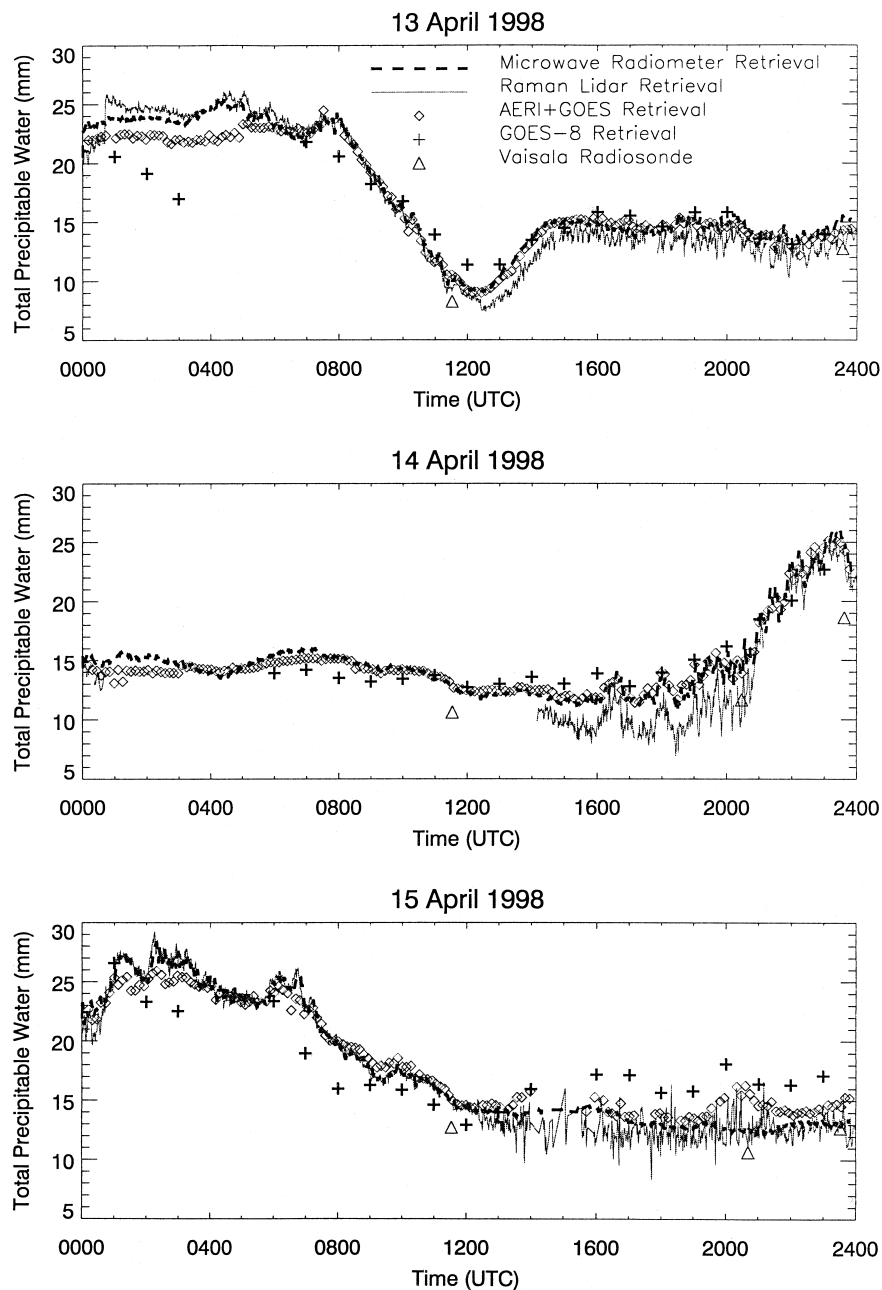

FIG. 12. Total precipitable water vapor time series from the Raman lidar, AERI+GOES, GOES, microwave radiometer, and the unscaled Vaisala radiosondes for 13–15 April 1998. The temporal resolution differs by instrument type with microwave radiometer and Raman lidar at 1 min, AERI+GOES at 10 min, GOES at hourly, and the Vaisala radiosondes are periodic. Notice the high correlation between AERI+GOES, microwave radiometer, and the Raman lidar in time along with the known dry bias within the radiosondes.

water vapor fields (Figs. 14b,c). There are differences between the AERI+GOES and Raman water vapor fields especially at the time of the frontal passage. Notice that the high water vapor amounts at 0.5–1.0 km identify the nose of the cold frontal system very well within the Raman data. This is not depicted as well within the AERI+GOES retrieval data due to the

reduction of vertical resolution and sensitivity with altitude as well as the relatively small thickness of the elevated moisture layer. It is believed that the AERI retrieval vertical resolution can be improved with the implementation of a higher vertical resolution "fast model" (Smith et al. 1999), and with the use of recently improved water vapor line measurements in other regions of the spectrum, not yet employed in the algorithm.

The complementary nature of using passive interferometry for temperature profiling and active Raman lidar for water vapor profiling (due to its higher vertical resolution) is indicated in Figs. 14a and 14c. It is quite evident that the moisture plume at 1 km, seen in the Raman lidar data between 1000 and 1500 UTC, is located under a strong temperature inversion at 1.5 km, as highlighted in Fig. 14a during this same period of time. By combining the AERI-derived temperature field and Raman water vapor mixing ratio field a relative humidity can be calculated (Fig. 14d). Since both aerosol backscatter and extinction coefficients can be derived independent from each other using the Raman lidar (Ferrare et al. 1998a), these profiles can be used with the relative humidity data to study the physical characteristics of aerosols such as size and composition (Ferrare 1997; Ferrare et al. 1998b; Ferrare et al. 1999). For example, note the increase in aerosol extinction between the surface and 1.0 km between 0800 and 0900 UTC. For this brief period, the water vapor mixing ratio measured by the Raman lidar remained nearly constant at 12 g kg^{-1} indicating that the increase in aerosol extinction with altitude was most likely due to hygroscopic growth rather than advection of different air masses. Since the temperature decreased 3–4 K between the surface and 1 km, the relative humidity increased from 70% to greater than 90% at 1 km leading to a 60%–70% increase in aerosol extinction between the surface and 1 km.
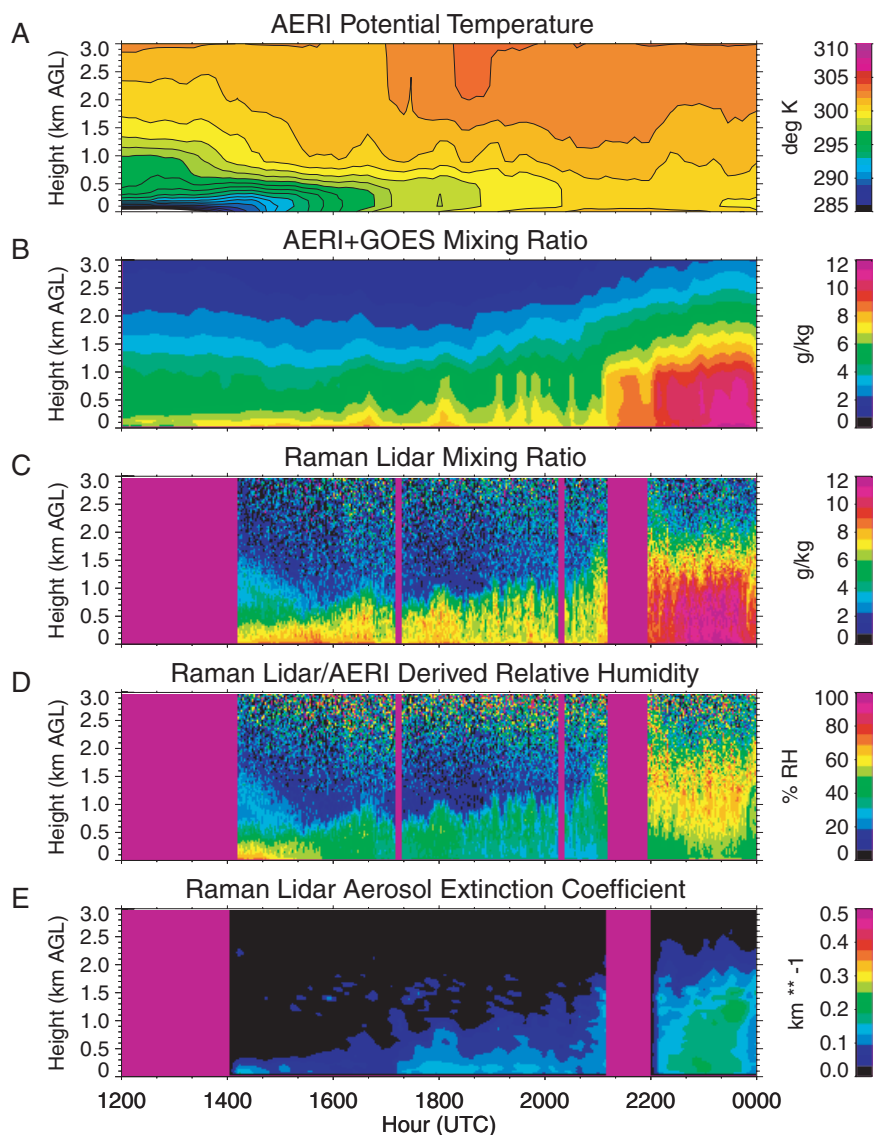

FIG. 13. Time–height cross sections of potential temperature derived from (a) the AERI, (b) water vapor mixing ratios derived from the (b) AERI+GOES and (c) Raman lidar, (d) relative humidity derived using AERI temperature and Raman lidar mixing ratio data, and (e) aerosol extinction from the Raman lidar 14 April 1998 from 1200 to 0000 UTC. Raman lidar water vapor data have been processed to have the maximum 1-min, 39-m resolution to view the finescale structure of the moisture field on this day; however, the aerosol data have a 10-min temporal resolution. The warm air advection event is included by the rapid return of deep moisture at 2100 UTC. Prior to this, pulses of increasing and decreasing moisture are indicated and highly correlated in time within the Raman lidar and AERI+GOES water vapor time–height cross sections.

5. Discussion and conclusions

The Department of Energy's Atmospheric Radiation Measurement program has provided

a unique opportunity to rapidly advance remote sensing capabilities for the atmospheric sciences and weather forecasting. Active Raman lidar and passive AERI systems are automated, environmentally hardened instruments capable of profiling water vapor at high temporal resolution and can continually map the planetary boundary layer water vapor structure. In addition, temperature can be derived from AERI radiances and aerosol extinction and backscatter profiles can be directly retrieved from the Raman lidar. Fractional water vapor differences of less than 5% at night and 10% during the day have been determined when comparing retrievals from the two instruments. The known dry bias of radiosonde's moisture measurement was verified by comparisons to the Raman lidar and AERI. We are able to reduce this bias by scaling the radiosonde's moisture profile, making the concurrent radiosonde total precipitable water values agree with microwave radiometer measurements. Several case studies indicate good correlation between the passive and active water vapor measurements.

The placement of the AERI and Raman lidar systems within close proximity of one another has provided long-term validation of AERI derived water vapor profiles. The resultant improvement to the AERI retrieval algorithm, and the installation of additional AERI systems at the ARM boundary facilities, located radially approximately 180 km away from the central facility, are providing site-wide coverage of temperature and moisture. The value of 10-min resolution convective stability indices and the severe thunderstorm nowcasting from this grid of AERI systems is being accessed. Other research is focused on the positive impact

these data, when combined with remotely sensed winds, have on mesoscale modeling.

The impact of the CART Raman lidar's ability to profile both water vapor and aerosols simultaneously is under investigation. For example, the lidar was able to capture aerosol and water vapor information that was most likely associated with smoke from fires in Mexico and Central America that was transported over the SGP domain during 12–21 May 1998 (Peppler
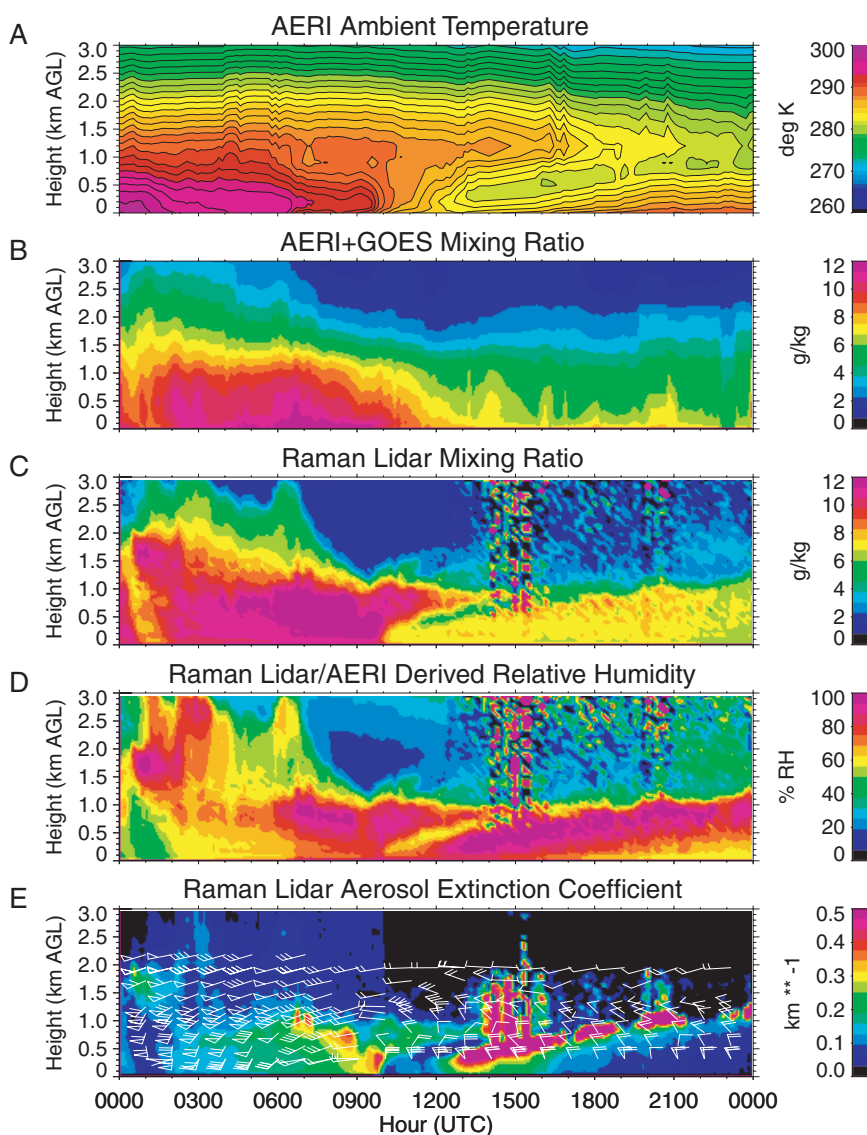

FIG. 14. Time–height cross sections of ambient temperature derived from (a) the AERI, water vapor mixing ratios derived from (b) the AERI+GOES and (c) Raman lidar, (d) relative humidity derived using AERI temperature and Raman lidar mixing ratio data, and (e) aerosol extinction from the Raman lidar for the 15 Apr 1998 cold front passage case. Both the AERI+GOES and the Raman lidar retrievals are at 10-min resolution. Wind data from a collocated 915-MHz wind profiler are overplotted on the aerosol data. The surface cold frontal passage is evident at 1000 UTC within the AERI+GOES temperature and Raman lidar water vapor fields.

et al. 2000, manuscript submitted to *Bull. Amer. Meteor. Soc.*). This instrument provides a very natural choice for validating water vapor and aerosol retrievals from the National Aeronautics and Space Administration's Moderate-Resolution Imaging SpectroRadiometer and Multi-Angle Imaging SpectroRadiometer instruments that are being flown on *Terra* (launched in December 1999), as well as the Total Ozone Mapping Spectrometer aerosol retrievals. Most of these retrievals based upon satellite data are sensitive to the vertical distribution of aerosols and the climatology of this distribution. Ongoing work focuses on identifying the climatology of the vertical aerosol distribution at the SGP CART site, as well as studying the relationship between relative humidity and its affect on the physical characteristics of atmospheric aerosols.

The synergy of the remote sensing methods provides unique state-of-the-atmosphere information in noncloudy skies used for a variety of atmospheric research applications. These new technologies represent an important advancement in understanding planetary boundary layer processes.

More information about the ARM project, as well as data from the Raman lidar and AERI, can be found on the ARM Web page (http://www.arm.gov).

References

Clough, S. A., F. X. Kneizys, L. S. Rothman, and W. O. Gallery, 1981: Atmospheric spectra transmittance and radiance: FASCODE1B. *Proc. Society of Photo-Optical Instrumentation Engineers,* **277,** 152–166.

——, P. D. Brown, D. D. Turner, T. R. Shippert, J. C. Liljegren, D. C. Tobin, H. E. Revercomb, and R. D. Knuteson, 1999: Effect on calculated spectral surface radiances due to MWR scaling of sonde water profiles. *Proc. Ninth Atmospheric Radiation Measurement (ARM) Science Team Meeting,* San Antonio, TX, U.S. Department of Energy. [Available online at http://www.arm.gov/docs/documents/technical/conf_9903/clough-99.pdf.]

Feltz, W. F., 1994: Meteorological applications of the atmospheric emitted radiance interferometer (AERI). M.S. thesis, Dept. of Atmospheric and Oceanic Sciences, University of Wisconsin—Madison, 87 pp. [Available from Memorial Library, 728 State St., Madison, WI 53703.]

——, W. L. Smith, R. O. Knuteson, H. E. Revercomb, H. M. Woolf, and H. B. Howell, 1998: Meteorological applications of temperature and water vapor retrievals from the ground-based atmospheric emitted radiance interferometer (AERI). *J. Appl. Meteor.,* **37,** 857–875.

Ferrare, R. A., 1997: The applicability of a scanning Raman lidar for measurements of aerosols and water vapor. Ph.D. Thesis, University of Maryland, 157 pp. [Available from University Library, College Park, MD 20742-7011.]

——, S. H. Melfi, D. N. Whiteman, and K. D. Evans, 1992: Raman lidar measurements of Pinatubo aerosols over southeastern Kansas during November–December 1991. *Geophys. Res. Lett.,* **19,** 1599–1602.

——, ——, ——, ——, F. J. Schmidlin, and D. O'C. Starr, 1995: A comparison of water vapor measurements made by Raman lidar and radiosondes. *J. Atmos. Oceanic Technol.,* **12,** 1177–1195.

——, ——, ——, ——, and R. Leifer, 1998a: Raman lidar measurements of aerosol extinction and backscattering: Methods and comparisons. *J. Geophys. Res.,* **103,** 19 663–19 672.

——, ——, ——, ——, M. Poellot, and Y. J. Kaufman, 1998b: Raman lidar measurements of aerosol extinction and backscattering: Derivation of aerosol real refractive index, single-scattering albedo, and humidification factor using Raman lidar and aircraft size distribution measurements. *J. Geophys. Res.,* **103,** 19 673–19 689.

——, D. D. Turner, L. A. Heilman, and W. F. Feltz, 1999: CART Raman lidar retrievals of aerosol extinction and relative humidity profiles. *Proc. 9th Atmospheric Radiation Measurement (ARM) Science Team Meeting,* San Antonio, TX, U.S. Department of Energy. [Available online at http://www.arm.gov/docs/documents/technical/conf_9903/ferrare-99.pdf.]

Goldsmith, J. E. M., F. H. Blair, S. E. Bisson, and D. D. Turner, 1998: Turn-key Raman lidar for profiling atmospheric water vapor, clouds, and aerosols. *Appl. Opt.,* **37,** 4979–4990.

Guichard, F., D. Parsons, and E. Miller, 2000: Thermodynamic and radiative impact of the correction of sounding humidity bias in the Tropics. *J. Climate,* in press.

Lesht, B. M., 1997: An internal analysis of SGP/CART radiosonde performance during the September 1996 water vapor intensive observation period. *Proc. 7th Atmospheric Radiation Measurement (ARM) Science Team Meeting,* San Antonio, TX, U.S. Department of Energy, 59–62. [Available online at http://www.arm.gov/docs/documents/technical/conf_9703/lesht_97.pdf.]

——, and J. C. Liljegren, 1996: Comparisons of precipitable water vapor measurements obtained by microwave radiometry and radiosondes at the Southern Great Plains Cloud and Radiation Testbed site. *Proc. 6th Atmospheric Radiation Measurement (ARM) Science Team Meeting,* San Antonio, TX, U.S. Department of Energy, 165–168. [Available online at http://www.arm.gov/docs/documents/technical/conf_9603/lesh_96.pdf.]

Liljegren, J. C., 1995: Observations of total column precipitable water vapor and cloud liquid water using a dual-frequency microwave radiometer. *Microwave Radiometry and Remote Sensing of the Environment,* D. Solimini, Ed., VSP, 107–118.

——, 1999: Automatic self-calibration of ARM microwave radiometers. *Microwave Radiometry and Remote Sensing of the Earth's Surface and Atmosphere,* P. Pampaloni and S. Paloscia, Eds., VSP.

Melfi, S. H., D. N. Whiteman, and R. A. Ferrare, 1989: Observation of atmospheric fronts using Raman lidar moisture measurements. *J. Appl. Meteor.,* **28,** 789–806.

Menzel, W. P., F. C. Holt, T. J. Schmit, R. M. Aune, A. J. Schreiner, G. S. Wade, and D. G. Gray, 1998: Application of *GOES-8/9* soundings to weather forecasting and nowcasting. *Bull. Amer. Meteor. Soc.,* **79,** 2059–2077.

Revercomb, H. E., D. D. LaPorte, W. L. Smith, H. Buijs, D. G. Murcray, and L. A. Sromovsky, 1988: High-altitude measurements of upwelling IR radiance: Prelude to FTIR from geosynchronous satellite. *Mikrochim. Acta,* **11,** 439–444.

——, F. A. Best, R. G. Dedecker, T. P. Dirkx, R. A. Herbsleb, R. O. Knuteson, J. F. Short, and W. L. Smith, 1993: Atmospheric Emitted Radiance Interferometer (AERI) for ARM. Preprints. *Fourth Symp. on Global Climate Change Studies,* Anaheim, CA, Amer. Meteor. Soc., 46–49.

Smith, W. L., 1970: Iterative solution of the radiative transfer equation for the temperature and absorbing gas profile of an atmosphere. *Appl. Opt.,* **9,** 1993–1999.

——, W. F. Feltz, D. H. Deslover, and H. B. Howell, 1998: ARM science applications of AERI measurements: 1997 progress. *Proc. 8th Atmospheric Radiation Measurement (ARM) Science Team Meeting,* Tucson, AZ, U.S. Department of Energy, 705–709. [Available online at http://www.arm.gov/docs/documents/technical/conf_9803/smith-98.pdf.]

——, ——, R. O. Knuteson, H. E. Revercomb, H. B. Howell, and H. M. Woolf, 1999: The retrieval of planetary boundary layer structure using ground-based infrared spectral radiance measurements. *J. Atmos. Oceanic Technol.,* **16,** 323–333.

Stokes, G. M., and S. E. Schwartz, 1994: The Atmospheric Radiation Measurement (ARM) program: Programmatic background and design of the Cloud and Radiation Testbed. *Bull. Amer. Meteor. Soc.,* **75,** 1201–1221.

Turner, D. D., and J. E. M. Goldsmith, 1999: 24-hour Raman lidar measurements during the Atmospheric Radiation Measurement program's 1996 and 1997 water vapor intensive observation periods. *J. Atmos. Oceanic Technol.,* **16,** 1062–1076.

——, T. R. Shippert, P. D. Brown, S. A. Clough, R. O. Knuteson, H. E. Revercomb, and W. L. Smith, 1998: Long-term analysis of observed and line-by-line calculations of longwave surface spectral radiance and the effect of scaling the water vapor profile. *Proc. 8th Atmospheric Radiation Measurement (ARM) Science Team Meeting,* Tucson, AZ, U.S. Department of Energy, 773–776. [Available online at http://www.arm.gov/docs/documents/technical/conf_9803/turner-98.pdf.]

Vaughan, G., D. P. Waring, L. Thomas, and V. Mitev, 1988: Humidity measurements in the free troposphere using Raman backscatter. *Quart. J. Roy. Meteor. Soc.,* **114,** 1471–1484.

Weber, B. L., and Coauthors, 1990: Preliminary evaluation of the first NOAA demonstration network wind profiler. *J. Atmos. Oceanic Technol.,* **7,** 909–918.

Whiteman, D. N., S. H. Melfi, and R. A. Ferrare, 1992: Raman lidar system for the measurement of water vapor and aerosols in the earth's atmosphere. *Appl. Opt.,* **31,** 3068–3082.

——, W. F. Murphy, N. W. Walsh, and K. D. Evans, 1993: Temperature sensitivity of an atmospheric Raman lidar system based upon a XeF excimer laser. *Opt. Lett.,* **18,** 247–249.

Xia, M. L., T. J. Schmit, and W. L. Smith, 1999: A nonlinear physical retrieval algorithm—Its application to the *GOES-8/9* sounder. *J. Appl. Meteor.,* **38,** 501–513.